JMEPEG
DOI: 10.1007/s11665-015-1801-x

1059-9495/$19.00

Electroless Ni-P/SiC Nanocomposite Coatings With Small Amounts of SiC Nanoparticles for Superior Corrosion Resistance and Hardness

Mohammad Islam, Muhammad Rizwan Azhar, Yasir Khalid, Rawaiz Khan, Hany S. Abdo, Mushtaq A. Dar, Olamilekan R. Oloyede, and T. David Burleigh

(Submitted August 10, 2015; in revised form September 22, 2015)

The addition of silicon carbide (SiC) nanoparticles into electroless nickel (Ni)-based coatings improves both corrosion resistance and mechanical properties of the resulting Ni-P/SiC nanocomposite coatings, making them potential candidate as protective coatings in aggressive environments. Ni-P/SiC nanocomposite coatings were produced from precursor bath with small SiC loading levels (0.25 or 1.0 g/L) and characterized for morphology, corrosion resistance, and hardness. Microstructural examination using FE-SEM and AFM revealed that incorporation of uniformly dispersed SiC nanoparticles leads to smaller nodule size with fine-grain structure and low surface roughness. Electrochemical impedance spectroscopy studies in 4 wt.% NaCl solution showed that the nanocomposite coatings exhibit excellent corrosion resistance, as indicated by high charge-transfer resistance and low double-layer capacitance values of ~137 kΩ cm^2 and 19 μF cm^{-2}, respectively. The coatings maintained their structural integrity even after 5 days of saline bath immersion, as there was no cracking in the deposit microstructure besides formation of shallow pits and submicron-sized pores. A two-fold increase in the average hardness value was noticed from 4.5 (pure Ni-P) to 8.5 GPa (Ni-P/SiC coating) which can be ascribed to modified deposit morphology and uniformly dispersed SiC nanoparticles that act as obstacles to plastic deformation.

Keywords EIS, electroless process, nanocomposite coatings, nanoindentation, SiC nanoparticles

1. Introduction

Owing to the exceptional physical and chemical properties such as hardness, wear resistance, ability to withstand thermal and cyclic stresses, corrosion resistance, and to disguise surface irregularities, electroless nickel-based composite coatings have been employed for a broad range of applications in engineering industries. Due to precise process control and the ability to obtain diverse morphologies, the process has gained widespread use in surface coatings, lithium ion batteries, catalysis, hydrogen production, and data storage applications (Ref 1-9). Electroless process involves synthesis of metal and/or alloy coatings or particles using a precursor solution without applying external current. In contrast with electroplating, the coatings are conformal with thickness uniformity even over intricate shapes. The reduction of nickel ions to metallic state necessitates use of an appropriate reducing agent that undergoes catalytic dehydrogenation during coating cycle. Among different types, sodium hypophosphite (NaH_2PO_2) is the most commonly used reducing agent. During the process, the overall chemical reaction involving catalytic dehydrogenation and nickel reduction is given by Eq 1

$$2H_2PO_2^- + 2H_2O + Ni^{2+} \rightarrow Ni + 4H^+ + 2HPO_3^- + H_2 \quad \text{(Eq 1)}$$

The elemental phosphorus is also codeposited through a secondary reaction via hydride ion or atomic hydrogen mechanism, represented by Eq 2 and 3, respectively.

$$2H_2PO_2^- + 2H^- \rightarrow 2\,P + 4OH^- + H_2 \quad \text{(Eq 2)}$$

$$4H_2PO_2^- \rightarrow 2\,P + 2OH^- + H_2 + 2H_2PO_3^{2-} \quad \text{(Eq 3)}$$

Thus, codeposition of phosphorus also occurs during coating growth, and nickel-phosphorus (Ni-P) coatings with low (1-5), medium (6-9), and high (>10) P weight percent can be produced depending on the bath constituents. The latter two coating types are amorphous or microcrystalline in the as-

Mohammad Islam, Yasir Khalid, and **Mushtaq A. Dar**, Center of Excellence for Research in Engineering Materials (CEREM), Advanced Manufacturing Institute, King Saud University, P. O. Box 800, Riyadh 11421, Saudi Arabia; **Hany S. Abdo**, Center of Excellence for Research in Engineering Materials (CEREM), Advanced Manufacturing Institute, King Saud University, P. O. Box 800, Riyadh 11421, Saudi Arabia and Mechanical Design and Materials Department, Faculty of Energy Engineering, Aswan University, Aswan, Egypt; **Muhammad Rizwan Azhar**, Chemical Engineering Department, Curtin University, Bentley, WA 6102, Australia; **Rawaiz Khan**, Department of Chemical Engineering, College of Engineering, King Saud University, P. O. Box 800, Riyadh 11421, Saudi Arabia; **Olamilekan R. Oloyede**, Institute for Materials Research (IMR), School of Chemical and **T. David Burleigh**, Materials and Metallurgical Engineering Department, New Mexico Institute of Mining and Technology, Socorro, NM 87801. Contact e-mails: mohammad.islam@gmail.com, miqureshi@ksu.edu.sa, rizwanazharr@yahoo.com, yasirkhalid728@hotmail.com, ykhalid@ksu.edu.sa, rawaiz_khan86@yahoo.com, enghany2000@yahoo.com, mdar@ksu.edu.sa, engrlekanoloyede@yahoo.com, and burleigh@nmt.edu.

Published online: 24 November 2015

deposited state and are generally heat treated to about 400 °C for the improvement in crystallinity and hardness. The effect of several parameters such as substrate condition (average surface roughness, pre-treatment for surface activation, application of an interlayer), precursor solution parameters (bath composition and pH, deposition temperature, time), agitation mechanism (magnetic stirring, ultrasonic vibration, circulation) on the composition, morphology, mechanical properties, and/or corrosion resistance of the coatings has been investigated (Ref 4, 10).

The electroless composite coatings can be produced via co-deposition of particles during coating growth. In this case, the particles get physically adsorbed to the coating growth front and are eventually embedded into the Ni-P alloy matrix. The particulate addition enhances structural and/or functional properties of these composite coatings that in turn possess a combination of characteristics from metallic matrix and inorganic particles. Different means for the incorporation of the particles into the metallic matrix include convection, mechanical entrapment, and electrophoretic migration to the growth front. The extent of particle addition depends on a number of factors including particle characteristics (size, shape, type, and concentration), precursor bath composition (constituents, pH, and temperature), and hydrodynamics (laminar, turbulent or mixed flow regimes) (Ref 9). Two main points are to be kept in mind while incorporating particles into the metallic matrix: (i) Increasing the particle loading in the bath will enhance the degree of particle incorporation into the metallic matrix to a certain extent, beyond which there will be no significant increase in the content of added particles and (ii) as the size of the particles to be co-deposited is reduced, the corresponding increase in their surface area will pose challenges of de-agglomeration and uniform dispersion within the matrix phase. The latter challenge is usually addressed by employing ultrasonic vibration and/or using an appropriate surfactant for particle surface modification in order to mitigate agglomeration. However, the addition of a surfactant not only increases the cost but also makes the coating process more difficult (Ref 11).

The electroless Ni matrix composite coatings can be produced by incorporating inorganic (alumina, silica, zirconia, silicon carbide) and/or organic (polytetrafluoroethylene, molybdenum disulfide, carbon nanostructures) nanoparticles (Ref 12-16). The choice of solid particles during codeposition depends on the specific application. Silicon carbide possesses the characteristics of both organic and inorganic components and exhibits distinguishing properties like exceptional erosion and wear resistance to find application in the automotive (i.e., engine parts such as rotor tips and piston internal combustion surfaces) and the aerospace industries (i.e., replacement for hard chrome coatings) (Ref 17, 18). Since the incorporation of silicon carbide particles influences bath chemistry, microstructure, and porosity of the coatings, process control is important to obtain desirable properties such as hardness, durability, corrosion resistance, and wear properties.

For both as-deposited and heat-treated coatings, the effect of silicon carbide (SiC) particles has been investigated on their corrosion resistance. For AZ91D magnesium alloy, the Ni-P/SiC coatings at 5.2 pH were found to offer superior corrosion and wear resistance (Ref 19). Another report investigated the effect of micron- and nanometer-size particles on cavitation erosion of the composite coatings over steel substrate (Ref 20). Any improvement in coating density and microstructure causes enhanced corrosion resistance in the as-plated as well as heat-treated samples (Ref 21). The presence of different corrosive environments (i.e., sodium chloride, sodium hydroxide or sulfuric acid) on coatings with SiC nanoparticles concentration in the range of 0-12 g/L, when prepared with or without surfactant, showed no particular trend; however, hardness values increased almost linearly with increasing SiC nanoparticles loading level (Ref 22).

Most of the reported work on Ni-P/SiC composite coatings employs relatively high particle loadings in the bath, on the order of several g/L, with micrometer- or nanometer-sized particles (Ref 20-23). The addition of fine silicon carbide nanoparticles at high loading levels necessitates the use of an appropriate surfactant for good dispersion in the bath. In this paper, we present results from electroless deposition of Ni-P and Ni-P/SiC composite coatings over polished copper substrates. Ni-P/SiC nanocomposite coatings were produced with 0.25 or 1.0 g/L of the SiC nanoparticles in the plating solution. Electrochemical impedance spectroscopy (EIS) studies were performed in 4 weight percent sodium chloride solution for maximum immersion time of 14 days. Nanoindentation and atomic force microscopy of the coatings was performed to assess the effect of SiC on overall coating hardness and topography.

2. Materials and Methods

Analytical grade chemicals (Sigma Aldrich, purity ≥ 99.5%) were used in as-received form. The silicon carbide nanopowder (45-65 nm, CAS: 409-21-2) was procured from Nanoshel LLC and used as-received. The solution for the electroless process was prepared using nickel chloride ($NiCl_2$), sodium hypophosphite (NaH_2PO_2), sodium succinate ($C_4H_4Na_2O_4$), and sodium chloride (NaCl). Using 25×25 mm^2 finely polished copper coupons as a substrate, the surface cleaning involved the use of iso-propanol for the removal of any residues followed with a rinse with distilled water. Following that, the samples were immersed vertically into 200 ml solution at 90 °C in order to produce pure Ni-P or Ni-P/SiC coatings. The composite coatings were obtained over a ~3-μm-thick pre-coat of Ni-P coating. The SiC nanoparticles were initially suspended in water with nanoparticle dispersion ensured through ultrasonic vibration for 30 min followed by addition to the electroless bath. The processing conditions as well as the coating properties are given in Table 1.

The surface topography and composition of the coatings was assessed using field-emission scanning electron microscope (FE-SEM) (JEOL; JSM7600F) at 5 kV operating voltage and 4.5-mm working distance. The atomic force microscope (AFM) (Park Systems; XE100) was employed in the true non-contact mode to produce three-dimensional surface topographies from different area scans. The depth line profiles and the indentation curves were obtained with a loading force of 20 or 40 μN at loading/unloading speed of 1 μN/s and the values of hardness were estimated. For other coating samples, a nanoindentation system (Micro Materials; NanoTest Vantage) with Berkovich indenter was used after mounting the sample using a cyanoacrylate adhesive.

Electrochemical impedance spectroscopy (EIS) studies were performed over pure and composite Ni-P coatings in 4 wt.%

Table 1 Deposition conditions, hardness, and the equivalent circuit components for the Ni-P and Ni-P/SiC coatings from EIS studies in 4.0 wt.% NaCl solution

	Synthesis conditions						EIS parameters			
									R_{ct}, kΩ cm^2	
ID	NaH_2PO_2, g/L	SiC, g/L	Temp., °C	Time, min.	Wt./area, mg/cm^2	Hardness, GPa	R_s, Ω cm^2 1 day	C_{dl}, μF cm^{-2} 1 day	1 day	5 days
N_1	25	×	85	60	1.674	4.5	8.74	17.9	70.7	67.7
N_1C_1	25	0.25	90	60	1.473	6.7	8.02	22.6	137.3	54.6
N_1C_2	25	1.00	90	60	2.418	7.0	8.71	64.4	32.2	62.6
N_2C_2	10	1.00	90	60	1.612	8.5	11.4	28.0	44.1	38.0

NaCl solution. In a three-electrode configuration, the coated sample, a saturated calomel electrode (SCE), and a stainless steel piece were used as working electrode, reference electrode, and counter electrode, respectively. The cell was connected with a computer-controlled Autolab Potentiostat (PGSTAT20). The measurements were made at room temperature (25 °C) for open circuit potential (OCP) in the range of 10 mHz to 0.1 kHz with ±5 mV (peak to peak), a DC-biased potential, and impedance data acquisition rate of 10 points per decade change in frequency, whereas NOVA 1.8 software was used to analyze the data. The samples were tested for different immersion times. The samples were kept immersed in the NaCl solution in a glass container covered with aluminum foil to avoid evaporation.

3. Results and Discussion

3.1 Microstructure and Morphology

The electron microscope examination of the SiC nanoparticles, as shown in Fig. 1(a and b), reveals an irregular shape and disk-like morphology with large variations in size. Despite the presence of a few micrometer-sized particles presumably clusters formed due to agglomeration, a large proportion is in the sub-micrometer size range with values on the order of few tens of nanometers. The TEM microstructure (Fig. 1b) represents a large cluster formed by SiC nanoparticles that are almost spherical in shape and have an average size of ~35 nm.

The addition of 0.25 g/L silicon carbide nanoparticles into the electroless bath leads to their embedding into the Ni-P coatings. While the incorporation of silicon carbide nanoparticles causes a drop in the average size of spherical nodules, the average surface roughness is also observed to be decreased. Few nanoparticles can be seen embedded in the near-surface region of the round grains, as indicated by white arrows in Fig. 1(c). High-magnification view (Fig. 1d), however, also reveals the presence of fine, round pores with diameters of ~20-30 nm that are located preferably along the grain boundaries. Such pores and defects may have formed due to hydrogen gas evolution during coating deposition, through chemical reactions represented by Eq 1-3 in the Introduction section. Whereas hydrogen gas formation impedes coating growth at those particular points, its subsequent release causes the formation of a Ni-P and/or a Ni-P/SiC layer, leaving nanosized pores/defects in the coating mostly at the grain boundaries (Ref 9). Inadequate substrate pre-treatment, aged bath, low coating thickness, and post-deposition heat treatment are among the factors that give rise to porosity in the electroless

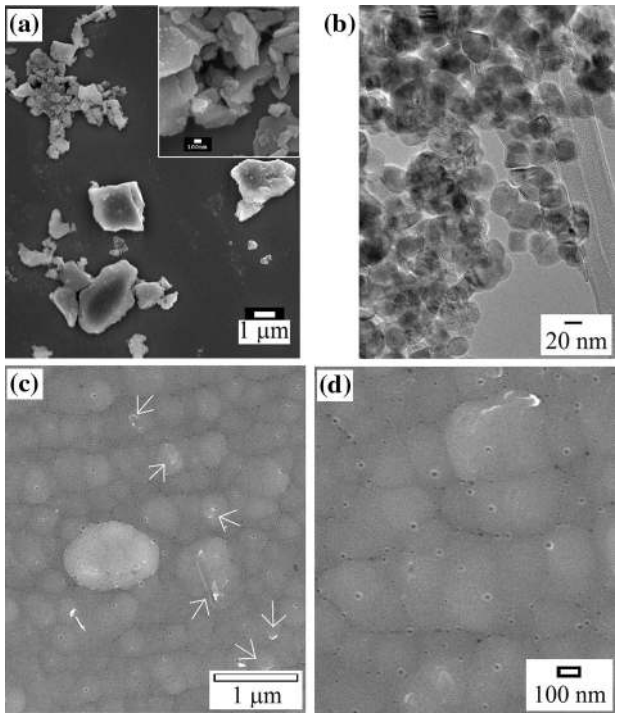

Fig. 1 (a) Low-magnification view of SiC nanoparticles (with inset showing high-magnification image of a cluster), (b) TEM microstructure of SiC nanoparticles (c, d) Low- and high-magnification images of the Ni-P/SiC nanocomposite coating (N_1C_1, 25 g/L NaH_2PO_2, 0.25 g/L SiC)

deposits, although Ni-P deposits containing P in excess of 10 weight percent exhibit less porosity. The presence of SiC nanoparticles on the growth front impedes further nucleation of the Ni and P from the solution, while at the same time, coating growth occurs due to autocatalytic action of the Ni-P coating surrounding the attached particle. Subsequently, the particles are also embedded in the coating at grain boundaries and/or near to the grain boundaries, causing the nodule size to be smaller than that of pure Ni-P coatings due to increased active nucleating sites (Ref 19). The presence of SiC particles in the coating was also qualitatively confirmed from EDS analysis. From a 30 × 30 μm area analysis, the respective weight percent values of P and SiC in the N_1C_2 sample (1.0 g/L SiC nanoparticles in the plating bath) were determined to be 13.7 and 0.6%, respectively.

The good conformation of the coating to the underneath substrate and dispersion of the added SiC particles is evident

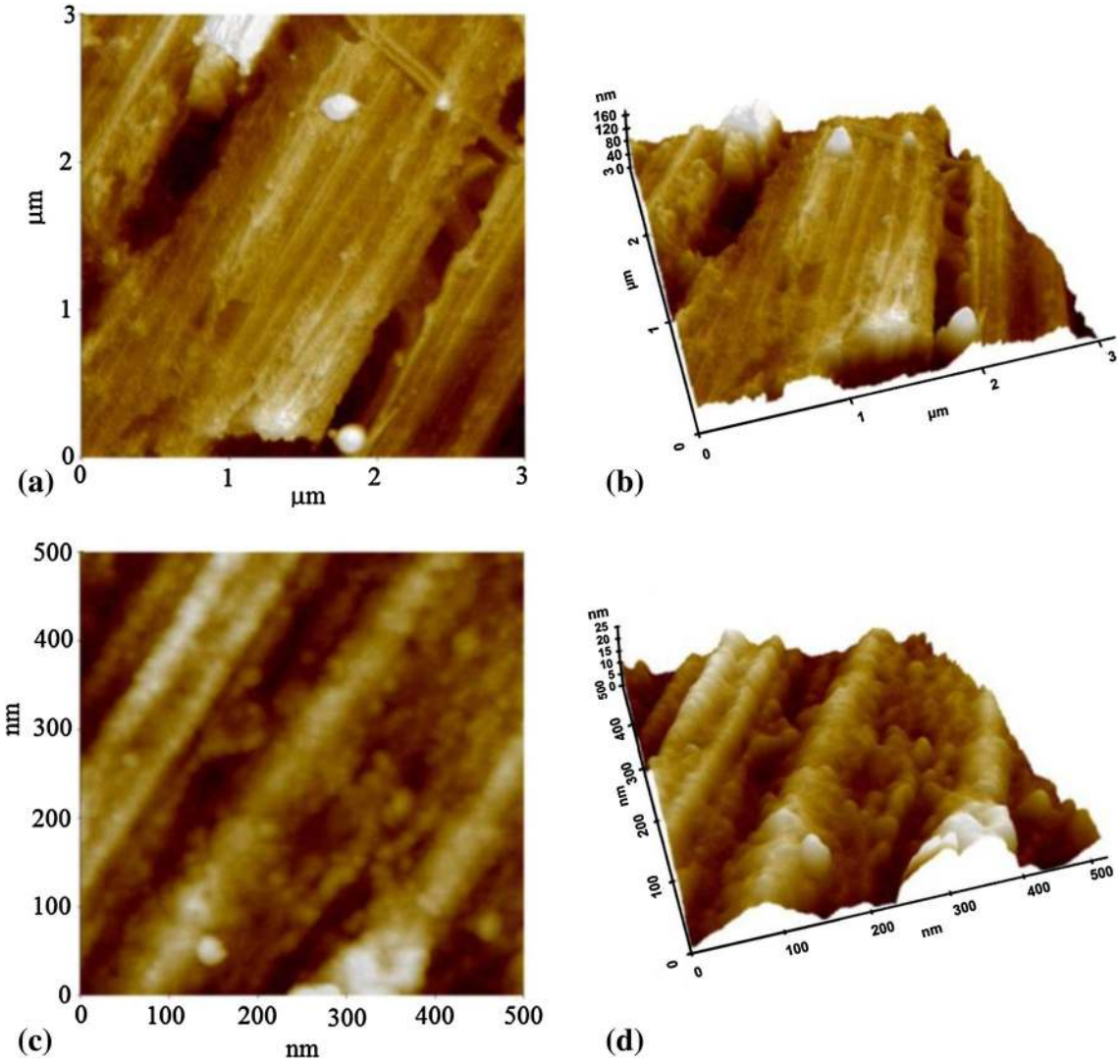

Fig. 2 Two- and three-dimensional surface morphology of the N_1C_2 coating (25 g/L NaH_2PO_2, 1.0 g/L SiC) with scan areas of (a, b) 3 × 3 µm and (c, d) 0.5 × 0.5 µm

from two- and three-dimensional morphologies of the N_1C_2 coating (Table 1), as shown in Fig. 2. From the area scans, the coating deposition within the scratches from grinding/polishing step is noticed, indicating conformal coverage of the substrate during growth. The effect of particulate addition on grain size refinement, as indicated by the small size of hemispherical-shaped grains, is also pronounced in the 500 × 500 nm scan. The maximum z-axis values of the AFM scans are 160 and 25 nm, respectively, revealing a relatively smooth surface morphology of the composite coatings. On the other hand, the Ni-P/SiC nanocomposite coating produced with the same SiC loading level (1.0 g/L) but with less sodium hypophosphite content of 10 g/L in the bath (N_2C_2) exhibits more smooth surface morphology with uniform dispersion of fine nanoparticles all over the surface as evident from Fig. 3(b). The effect of the particulate addition on grain size refinement is more pronounced in the case of sample N_1C_2 (Fig. 2d), as indicated by the small size of the hemispherical-shaped grains. Thus, despite the influence from the SiC nanoparticles addition, the amount of NaH_2PO_2 as reducing agent also affects the resulting deposit morphology. It is noteworthy that an increase in the reducing agent (NaH_2PO_2) content not only leads to high P incorporation into the deposit, the resulting coating is microcrystalline or amorphous with greater average surface roughness due to availability of more hypophosphite ions for reduction of Ni^{2+} in the bath.

3.2 Corrosion Properties

The electrochemical impedance spectroscopy (EIS) method is one of the prevailing procedures to study corrosion resistance of different coatings. For the neat Ni-P coating (sample N_1), the corrosion behavior after different immersion times in the 4 wt.% sodium chloride solution is represented by the Bode spectra and Nyquist plots in Fig. 4. The reason for presenting both types of data is to accurately analyze with minimum error in data interpretation. From the Bode spectra (Fig. 4a), it is evident that the coating exhibits superior corrosion resistance at the initial stage of exposure to the saline bath. The high-frequency regime of the Bode diagram reveals information

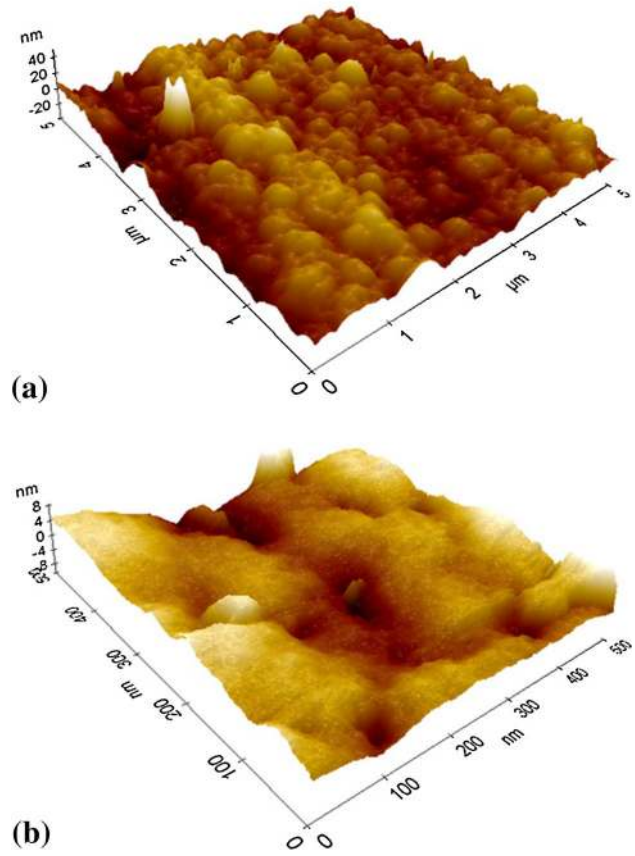

Fig. 3 Three-dimensional surface morphology of the N2C2 coating (10 g/L NaH_2PO_2, 1.0 g/L SiC) with scan areas of (a) 3 × 3 μm and (b) 0.5 × 0.5 μm

about possible coating defects formation and other changes in the surface area upon exposure, whereas the impedance at low frequencies is correlated with simultaneous physicochemical phenomena at the metal/coating interface (Ref 24). The presence of only one phase angle maximum (Fig. 4b) indicates one time constant in the spectra, thus implying coating deterioration over time without any occurrence of interfacial failure that could lead to coating delamination.

The EIS Nyquist plots recorded on the pure Ni-P coating at open circuit potential and for different immersion times are shown in Fig. 4(c). Immediately upon immersion into salt solution, there is a small capacitive loop at high frequency followed by a large capacitive loop at low frequency, implying pore fill up upon an initial interaction between coating and electrolyte. Prolonged immersion into a saline bath, however, results in only one capacitive loop in the whole frequency range, indicative of an ongoing reaction between coating and electrolyte and filling of the pores. A depression is noticed in the capacitive loops recorded at high frequency that may be attributed to surface morphology and presence of pores. For Ni-P coating, the corrosion resistance decreases at low frequency upon extended exposure to a salt bath, as evident from reduction in size of the capacitive loop. The reduction in corrosion resistance may be attributed to precipitation of chloride ions (Cl^-) on the coating surface once the saturation limit is reached. The Cl^- ions are aggressive for nickel and a critical concentration of ~0.002-0.02 M NaCl is required to cause pitting in the uninhibited NaCl solution (Ref 25). Nevertheless, the electrolyte can reach the substrate through a wetting process only after through-coating pores are formed by means of an interconnection of pores and/or coating delamination. The values of charge-transfer resistance (R_{ct}) and double-layer capacitance (C_{dl}), listed in Table 1, do not appear

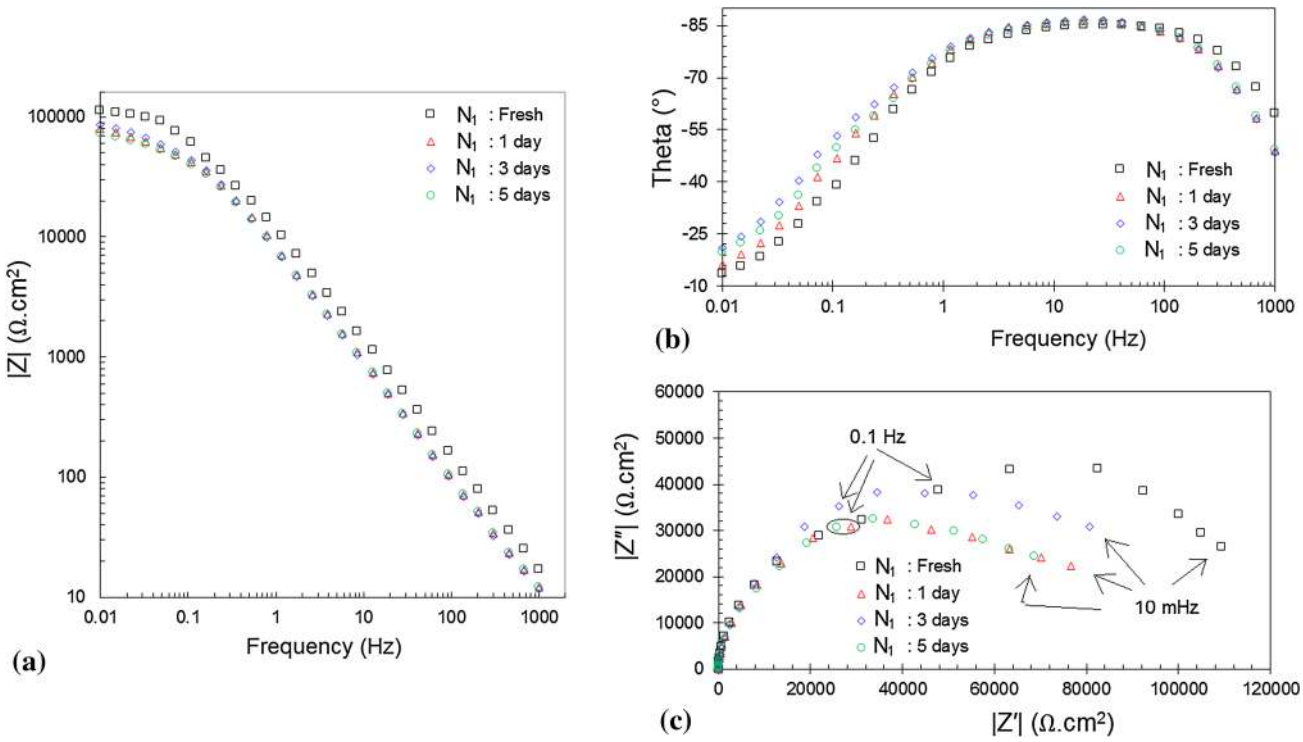

Fig. 4 EIS data for the neat Ni-P coating for different immersion times: (a, b) Bode diagrams and (c) Nyquist plots

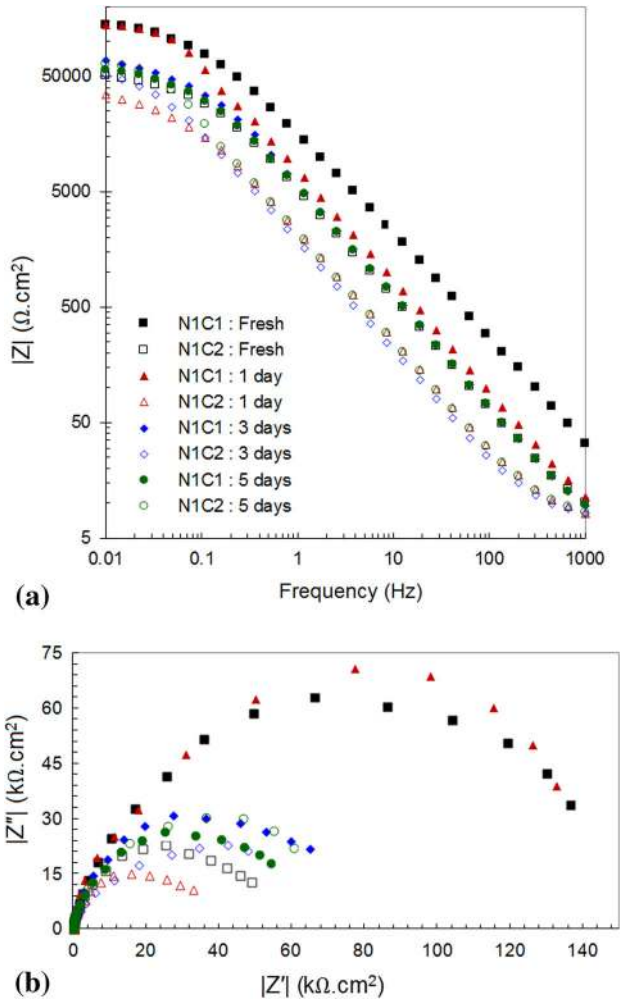

Fig. 5 EIS data for the composite Ni-P-SiC coatings obtained from 0.25 (N_1C_1) or 1.0 (N_1C_2) mg/L SiC nanoparticles in the plating solution: (a) Bode diagram and (b) Nyquist charts

to change drastically upon prolonged exposure indicating a small degree of coating deterioration over time. During exposure to the saline bath, the nickel in the Ni-P coating preferentially dissolves with hydration of nickel being the first step towards formation of either soluble Ni^{2+} species or passive nickel film in medium- and high-P coatings along with phosphorous enrichment. The chemical reaction between the enriched phosphorus surface and water leads to production of hypophosphite anions with consequent formation of an adsorbed layer that effectively blocks the supply of water molecules to the electrode surface, thereby enhancing the corrosion resistance of the Ni-P/SiC nanocomposite coating. The coating surface potentials are observed to be relatively stable, indicating a homogenous coating structure. From both Bode phase angle spectra and Nyquist plots, it is concluded that only one corrosion mechanism is prevalent in pure Ni-P coating.

The corrosion behavior of the composite coatings from EIS studies is presented in Fig. 5. The composite coating prepared from a plating solution with a low loading of silicon carbide particles (i.e., 0.25 g/L) exhibits superior corrosion resistance than that obtained from a higher silicon carbide loading level (1.0 g/L) in the bath, as suggested by higher area-impedance values for a relatively short immersion time of 24 h. For instance, the $|Z|_{max}$ values (at 10 mHz frequency) for N_1C_1 and N_1C_2 coatings after a 1 day immersion are on the order of 138 and 34 kΩ cm^2, respectively. The corrosion behavior of both coatings is similar for longer immersion periods. The enhancement in corrosion resistance of the composite coatings is contingent upon several factors including the effective metallic area susceptible to corrosion, the chemical stability of the embedded nanoparticles, the extent of porosity in the coating, and the knack to avert chloride ion diffusion into the metal/particle interface (Ref 26). The Nyquist charts (Fig. 5b) reveal the superior corrosion resistance of the N_1C_1 sample for immediate exposure and after 1 day immersion, as indicated by large diameters of the semicircles. For longer times, however, the corrosion behavior of the composite coatings is similar regardless of silicon carbide content in the coatings. From electrochemical parameters of the EIS data as determined in an attempt to fit the experimental data and listed in Table 1, the following observations are made: (i) the values of solution resistance are in the same range, i.e., 8-9 Ω cm^2 which implies that the saline bath condition does not vary significantly from one sample to the other; (ii) a comparison of the charge-transfer resistance values (also called polarization resistance) reveals that although these are in close proximity for prolonged exposure, the maximum and minimum values at the initial stage of exposure belong to the N_1C_1 and N_1C_2 coatings, respectively, and (iii) the electrical double-layer capacitance (C_{dl}) value for the N_1C_1 coating is slightly higher than those of N1 sample, whereas it is almost 2.5 times higher in case of N_1C_2 coating. The wide difference in the values of solution resistance and charge-transfer resistance dictates capacitive impedance with a phase angle approaching −90° which is confirmed from phase angle data (−81.5 and −85.2 for N_1C_1 and N_1C_2, respectively). Furthermore, a fourfold increase in the SiC particles loading in the precursor bath (from 0.25 to 1.0 g/L) enhances the degree of porosity in the coating, since it was observed that C_{dl} value, a measure of surface porosity in the coatings, progressively increased from ∼17.9 to 64.4 μF cm^{-2} for pure Ni-P to Ni-P/SiC produced with 1.0 g/L silicon carbide nanoparticles in the precursor bath. Electroless deposition from a bath containing higher silicon carbide nanoparticles loading, on the order of few grams per liter, raises issues related to dispersion in the metallic matrix and a tendency to form agglomerates by the second phase particles that subsequently influence microstructure and surface porosity, thus adversely affecting corrosion resistance.

The microstructure of the N_1C_1 sample was examined after immersion into 4 wt.% sodium chloride solution for 5 days, as shown in Fig. 6. The overall surface of the nanocomposite coating (Fig. 6a) is seen to represent two different surface morphologies indicative of variation in the severity of the corrosive environment along with the presence of submicron-sized pores. A closer look at the smooth region suggests the presence of round pores a few tens of nanometers in diameter, indicated by white circles, which presumably were at the surface and were enlarged during exposure to the saline bath. In addition, finer pores seem to appear on the coating surface. Beside pores, shallow pits were also formed (indicated by a diamond shape), presumably due to the SiC nanoparticle removal and subsequent penetration of the chloride ions. There are certain instances when both the pore and the pit formed due to silicon carbide nanoparticle removal are located in close proximity, as outlined by a rounded rectangle in Fig. 6(b). In essence, the smooth regions highlight the more protective

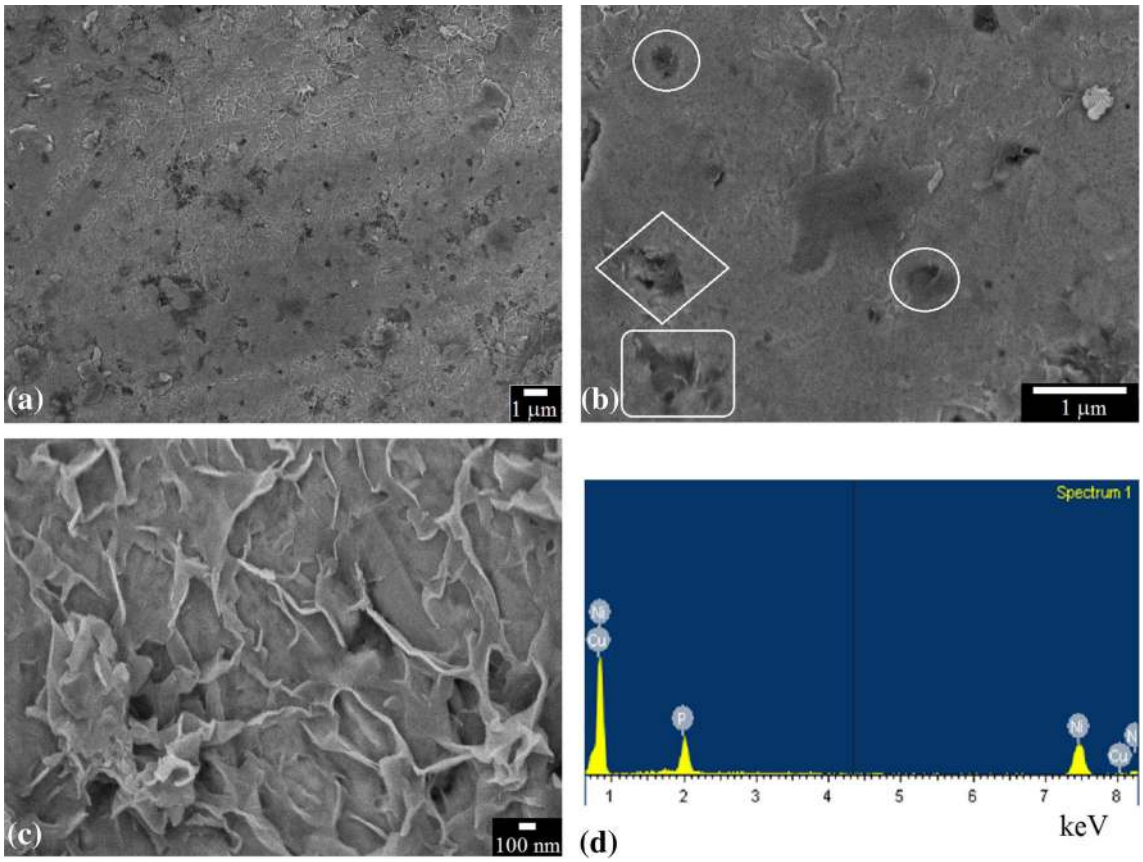

Fig. 6 FE-SEM microstructures of the Ni-P/SiC nanocomposite coating (N_1C_1) after 5 days immersion in 4 wt.% NaCl solution: (a) Overall surface at low magnification, (b) less corroded area with the presence of pits and pores, (c) rough coating microstructure indicative of more aggressive corrosion, and (d) EDS spectrum with peaks representative of coating constituents

Table 2 Corrosion characteristics and electrochemical parameters from EIS studies for Ni-P/SiC coatings

	Parameters	This work	(Ref 23)	(Ref 19)	(Ref 29)
SiC in bath (g/L)		0.25	6.0	4.0	2-8
Electrochemical parameters	C_{dl}, µF cm^{-2}	22.6	79.32	36.62	16.87
	R_{ct}, kΩ cm^2	137.6	24.787	31.326	13.27
Potentiodynamic polarization	i_{corr}, µA/cm^2	×	306	1.36	1.65
	E_{corr}, mV	×	−383	−382	−606
NaCl (wt.%)		4	3.5	3.5	3.5
Substrate		Copper	Carbon steel	Mg alloy (AZ91D)	Mild steel

nature of the nanocomposite coating with a preferential localized attack at surface defects such as pores and eroded silicon carbide nanoparticles. The microstructure shown in Fig. 6(c) indicates a rough, flaky morphology not reported in literature before. In contrast with microstructures obtained from corrosion of the pure Ni-P and Ni-P/SiO_2 nanocomposite (Ref 14) coatings, there is no crack formation in our case. Possible cause(s) for evolution of such morphology need to be further investigated. The EDS spot analysis (Fig. 6d) of the pit/pore area did not find any x-ray peaks characteristic of Si, implying removal of silicon carbide nanoparticles from the region.

Although potentiodynamic polarization studies were not performed during this work, it is pertinent that the results reported elsewhere are briefly summarized here in Table 2 along with comparison of our EIS data with recently reported work. As estimated from polarization curves, the values of corrosion current and corrosion potential are in the range of a few µA/cm^2 and ~400-600 mV, indicating towards good corrosion resistance of such coatings. Comparison of our electrochemical parameters with some of the reported values suggests that the performance attributes of our nanocomposite coatings are at par or superior to their counterparts containing much higher SiC nanoparticles content and in a relatively less aggressive environment.

3.3 Nanoindentation Studies

AFM and nanoindentation is used to find the hardness of pure and nanocomposite coatings. The influence of silicon carbide nanoparticles on the hardness values of Ni-P/SiC coatings is obvious; silicon carbide being one of the hardest

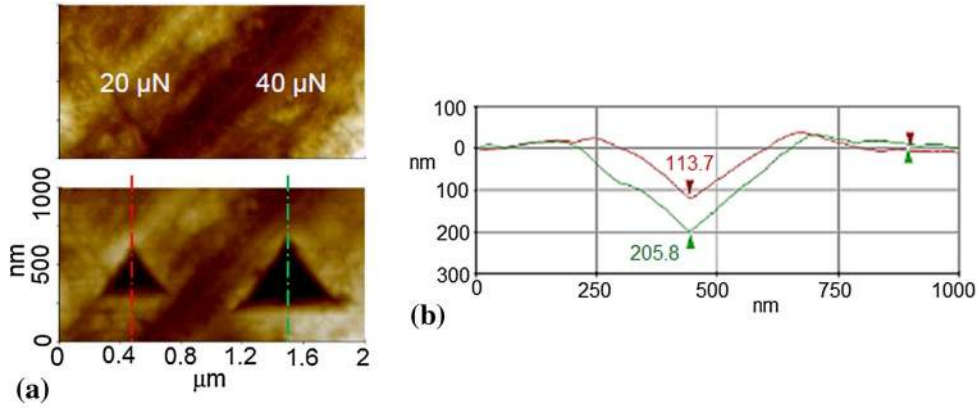

Fig. 7 (a) AFM area scans of the N_1C_2 nanocomposite coating surface before and after indentation tests and (b) the corresponding depth line profiles

materials resulted in improved hardness than pure Ni-P coatings. Recently, nanoindentation on silicon carbide coatings has been reported with hardness values as high as 20 GPa for silicon carbide grains while 9.5 GPa for silicon carbide coatings on silicon wafers (Ref 27). Actually, silicon carbide restricts plastic deformation of the coating. Figure 7 represents a hardness test perform using an AFM. It is clear that increasing the load resulted in a greater indent depth; however, it does not affect hardness values as the coating is quite thicker than the indent depth. The uniformity of the coatings and adhesion to the substrate results in a thermodynamically stable coating. From the indentation curve representing loading-unloading behavior, the value of elastic modulus for the N_1C_1 sample was determined to be ~1.3 GPa. Moreover, silicon carbide particles hinder the dislocation of the particles and results in improved hardness than pure Ni-P coatings. Some recent studies investigated the effect of SiC keeping pitting effects in consideration and reported hardness values of 6.9 GPa (Ref 9). However, in simulation studies for Ni-P-SiC coatings on a 6061 aluminum alloy, hardness has been reported as 6.5 GPa (Ref 28). In our case, hardness values are 6.7 GPa for N_1C_1 and 7.0 GPa for N_1C_2. The average hardness value for the N_2C_2 sample was the maximum at 8.5 GPa, which may be attributed to less amount of phosphorus in the coating matrix. The average values of the hardness for 12 indents for each sample are shown in Table 1. The linearity of microhardness as a function of silicon carbide content is not statistically substantial (Ref 29); nevertheless, a steady growth is observed on increasing the amount of silicon carbide. This is exactly in accordance with results presented in literature where the silicon carbide particles dispersion in the metal matrix indicated inhibiting effect on the grain growth, thus causing an increase in the hardness (Ref 30).

4. Conclusions

Electroless Ni-based nanocomposite coatings can be produced using small amounts of silicon carbide nanoparticles (0.25 and 1.0 g/L) in the precursor bath without any need of a dispersant. This SiC nanoparticles addition modifies the deposit morphology by reducing the size of the spherical nodules and the average surface roughness when examined using FE-SEM and AFM. EIS studies show that the best corrosion protection in a saline bath is achieved in case of nanocomposite coatings made from 1.0 g/L SiC nanoparticles in the bath. The electrochemical parameters determined from theoretical fit of the experimental data point towards superior corrosion properties with higher charge-transfer resistance (R_{ct}) and low double-layer capacitance (C_{dl}) values. The addition of SiC to the metallic matrix effectively passivates the nanocomposite coating structure in case of prolonged exposure, since no cracks were seen after prolonged exposure to the salt solution. Furthermore, SiC nanoparticles embedded in the nickel-phosphorus matrix act as barriers to plastic deformation with a maximum increase in the hardness value to 8.5 GPa.

Acknowledgments

The authors gratefully acknowledge the technical and financial support of the Research Center of College of Engineering, Deanship of Scientific Research, King Saud University.

References

1. T. Liu, L. Zhao, D. Wang, J. Zhu, B. Wang, and C. Guo, Corrosion Resistance of Nickel Foam Modified with Electroless Ni-P alloy as Positive Current Collector in a Lithium Ion Battery, *RSC Adv.*, 2013, **3**, p 25648–246851
2. Y. Lu, J.-K. Liu, X.-Y. Liu, S. Huang, T.-Q. Wang, X.-L. Wang, C.D. Gu, J.P. Tu, and S.X. Mao, Facile Synthesis of Ni-Coated Ni2P for Supercapacitor Applications, *Cryst. Eng. Comm.*, 2013, **15**, p 7071–7079
3. P. Sahoo and S.K. Das, Tribology of Electroless Nickel Coatings—A Review, *Mater. Des.*, 2011, **32**, p 1760–1775
4. M. Islam and O.T. Inal, Development of Electron Reflection Suppression Materials for Improved Thermionic Energy Converter Performance using Thin Film Deposition Techniques, *J. Appl. Phys.*, 2006, **100**, p 084903 (12 pages)
5. C. Fukuhara, R. Hyodo, K. Yamamoto, K. Masuda, and R. Watanabe, A Novel Nickel-Based Catalyst for Methane Dry Reforming: A Metal Honeycomb-Type Catalyst Prepared by Sol-Gel Method and Electroless Plating, *Appl. Catal. A*, 2013, **468**, p 18–25
6. D. Li, L. Wang, P. Zhang, S. Chen, and J. Xu, HI, Decomposition over PtNi/C Bimetallic Catalysts Prepared by Electroless Plating, *Int. J. Hydrogen Energy*, 2013, **38**, p 10839–10844
7. S.S. Muir, Z. Chen, B.J. Wood, L. Wang, G.Q. Lu, and X. Yao, New Electroless Plating Method for Preparation of Highly Active Co-B Catalysts for NaBH4 Hydrolysis, *Int. J. Hydrogen Energy*, 2014, **39**, p 414–425

8. K. Zeng, R. Stierman, D. Abbott, and M. Murtuza, The Root Cause of Black Pad Failure of Solder Joints with Electroless Ni/Immersion Gold Plating, *JOM*, 2006, **58**, p 75–79
9. Z. Qi, W. Lu, A. Guo, Y. Hu, W. Lee, and X. Zhang, Investigation on Circular Plating Pit of Electroless Ni-P Coating, *Ind. Eng. Chem. Res.*, 2014, **53**, p 3097–3104
10. S. Kundu, S.K. Das, and P. Sahoo, Properties of Electroless Nickel at Elevated Temperature-A Review, *Proc. Eng.*, 2014, **97**, p 1698–1706
11. N. Nwosu, A. Davidson, C. Hindle, and M. Barker, On the Influence of Surfactant Incorporation During Electroless Nickel Plating, *Ind. Eng. Chem. Res.*, 2012, **51**, p 5635–5644
12. M. Islam and T. Shehbaz, Effect of Synthesis Conditions and Post-Deposition Treatments on Composition and Structural Morphology of Medium-Phosphorus Electroless Ni-P Films, *Surf. Coat. Technol.*, 2011, **205**, p 4397–4400
13. S. Alirezaei, S.M. Monirvaghefi, A. Saatchi, M. Ürgen, and K. Kazmanlı, Novel Investigation on Tribological Properties of Ni-P-Ag-Al_2O_3 Hybrid Nanocomposite Coatings, *Tribol. Int.*, 2013, **62**, p 110–116
14. M. Islam, M.R. Azhar, N. Fredj, T.D. Burleigh, O.R. Oloyede, A.A. Almajid, and S.I. Shah, Influence of SiO_2 Nanoparticles on Hardness and Corrosion Resistance of Electroless Ni-P Coatings, *Surf. Coat. Technol.*, 2015, **261**, p 141–148
15. Y. Wu, H. Liu, B. Shen, L. Liu, and W. Hu, The Friction and Wear of Electroless Ni-P Matrix with PTFE and/or SiC Particles Composite, *Tribol. Int.*, 2006, **39**, p 553–559
16. M. Islam, M.R. Azhar, N. Fredj, and T.D. Burleigh, Electrochemical Impedance Spectroscopy and Indentation Studies of Pure and Composite Electroless Ni-P Coatings, *Surf. Coat. Technol.*, 2013, **236**, p 262–268
17. J.N. Balaraju, T.S.N. Sankara Narayanan, and S.K. Seshadri, Electroless Ni-P Composite Coatings, *J. Appl. Electrochem.*, 2003, **33**, p 807–816
18. G.O. Mallory and J.B. Hajdu, *Electroless Plating: Fundamentals and Applications*, Cambridge University Press, Cambridge, 1990, p 207–227
19. H.-L. Wang, L.-Y. Liu, Y. Dou, W.-Z. Zhang, and W.-F. Jiang, Preparation and Corrosion Resistance of Electroless Ni-P/SiC Functionally Gradient Coatings on AZ91D Magnesium Alloy, *Appl. Surf. Sci.*, 2013, **286**, p 319–327
20. C.J. Lin, K.C. Chen, and J.L. He, The Cavitation Erosion Behavior of Electroless Ni-P-SiC Composite Coating, *Wear*, 2006, **261**, p 1390–1396
21. F. Bigdeli and S.R. Allahkaram, An Investigation on Corrosion Resistance of As-Applied and Heat Treated Ni-P/NanoSiC Coatings, *Mater. Des.*, 2009, **30**, p 4450–4453
22. S. Zhang, K. Han, and L. Cheng, The Effect of SiC Particles Added in Electroless Ni-P Plating Solution on the Properties of Composite Coatings, *Surf. Coat. Technol.*, 2008, **202**, p 2807–2812
23. C. Ma, F. Wu, Y. Ning, and F. Xia, Effect of Heat treatment on Structures and Corrosion Characteristics of Electroless Ni-P-SiC Nanocomposite Coatings, *Ceram. Int.*, 2014, **40**, p 9279–9284
24. S. Ozkan, G. Hapçı, G. Orhan, and K. Kazmanl, Electrodeposited Ni/SiC Nanocomposite Coatings and Evaluation of Wear and Corrosion Properties, *Surf. Coat. Technol.*, 2013, **232**, p 734–741
25. M.M. Al-Abdallah, A.K. Maayta, M.A. Al-Qudah, and N.A.F. Al-Rawashdeh, Corrosion Behavior of Copper in Chloride Media, *Open Corros. J.*, 2009, **2**, p 71–76
26. K. Krishnaveni, T.S.N.S. Narayanan, and S.K. Seshadri, Corrosion Resistance of Electrodeposited Ni-B and Ni-B-Si3N4 Composite Coatings, *J. Alloy Compd.*, 2009, **480**, p 765–770
27. V. Cech, T. Lasota, E. Palesch, and J. Lukes, The Critical Influence of Surface Topography on Nanoindentation Measurements of a-SiC: H Films, *Surf. Coat. Technol.*, 2015, **261**, p 114–121
28. R. Soleimani, F. Mahboubi, S.Y. Arman, M. Kazemi, and A. Maniee, Development of Mathematical Model to Evaluate Microstructure and Corrosion Behavior of Electroless Ni-P/Nano-SiC Coating Deposited on 6061 Aluminum Alloy, *J. Ind. Eng. Chem.*, 2015, **23**, p 328–337
29. M. Franco, W. Sha, S. Malinov, and H. Liu, Micro-Scale Wear Characteristics of Electroless Ni-P/SiC Composite Coating under Two Different Sliding Conditions, *Wear*, 2014, **317**, p 254–264
30. C.F. Malfatti, H.M. Veit, C.B. Santos, M. Metzner, H. Hololeczek, and J.-P. Bonino, Heat Treated NiP–SiC Composite Coatings: Elaboration and Tribocorrosion Behaviour in NaCl Solution, *Tribol. Lett.*, 2009, **36**, p 165–173